Supplementary information available

Photocatalytic degradation of triclosan on Au-Cu_2O nanowire arrays under visible light irradiation

Junfeng Niu,[†] *Yunrong Dai* [†,‡], *Lifeng Yin*,[†,*] *Jianying Shang*[†], *John Charles Crittenden*[†,§]

[†] State Key Laboratory of Water Environment Simulation, School of Environment, Beijing Normal University, Beijing 100875, P. R. China

[‡] State Key Laboratory of Environmental Criteria and Risk Assessment, Chinese Research Academy of Environmental Sciences, Beijing 100012, P. R. China

[§] School of Civil and Environmental Engineering and the Brook Byers Institute for Sustainable Systems, Georgia Institute of Technology, Atlanta, GA 30332, United States

This supplementary information contains the detailed information on "Solid phase extraction.", "photoelectrochemical measurements", "ESR measurements", "Mechanism of Cu_2O rod formation", "Photoabsorptivity", "TOC difference under visible light and UV light.", "Kinetics", "Quantum yield of degradation", "Optimum amount of Au", "Catalytic role of gold", "ESR analysis", "Frontier Molecular Orbit", "Work Function", "E_{LUMO} of TCS", "Charge transfer direction upon irradiation", and Figures S1-S21.

In total, there are twenty one Figures, and the document length is twenty seven pages.

[*] Corresponding author. Tel. and fax: +86-10-5880 5853.
E-mail: lfyin@bnu.edu.cn (L. F. Yin).

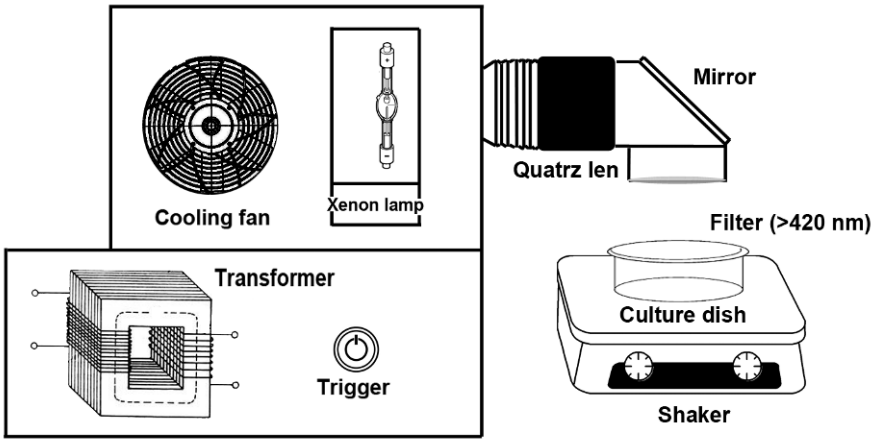

Figure S1. The set-up for the photocatalytic degradation of TCS by Au-Cu_2O NWAs.

Solid phase extraction. The Oasis HLB solid phase extraction columns (Waters, USA) were used to concentrate the intermediate products during the photocatalytic degradation of TCS. The columns were firstly activated with 5 mL of methanol. After loading 50 mL of reaction solution, the columns were eluted with 5 mL of mixture of acetonitrile and methanol (v:v=1:1),and the eluent was further concentrated into 0.2 mL by vacuum rotary evaporation (RV8V-C, IKA, GER). The concentrated samples were kept in the vials with glass-lined pipes at 5 °C in a refrigerator.

Photoelectrochemical measurements. A typical three-electrode setup was used for photoelectrochemical measurements. The electrolyte solution was 10 mg L^{-1} TCS in 0.1 mol L^{-1} NaOH. Prior to the measurement, the solutions were bubbled with nitrogen for 15 min. Platinum and Ag/AgCl were used as the auxiliary and reference electrodes, respectively. The Cu_2O NWAs or Au-Cu_2O NWAs grown on the Cu foil was used as the working electrode. Photocurrent measurements were controlled by a CHI660D electrochemical workstation (CH Instruments, CHN). A 1000-W Xe

lamp (Tmhhlight, CHN) in a Muller housing equipped with a cut-off filter at 420 nm (SCF-S50-42L; Sigma Koki, JPN) was used for visible light irradiation.

ESR measurements. ESR (electron spin resonance) were conducted at room temperature under the following conditions: center field of 3480 G; microwave power of 10.0 mW; receiver gain 100000; modulation frequency 100.0 kHz; modulation amplitude 2.07 G; conversion of 40.96 ms; sweep width 100.0 G; sweep time 41.9 s. The solution of 5, 5-dimethyl-1-pyrroline-N-oxide (DMPO) was used as the spin trap for superoxide (O_2^-) and •OH [1, 2]. The solution of 2,2,6,6-tetramethyl-4-hydroxy-piperidinyloxy (TEMP) was used to trap singlet oxygen ($^1O_2$) [3]. The time between the reaction initiation and the onset of ESR scanning was controlled to less than 2 min.

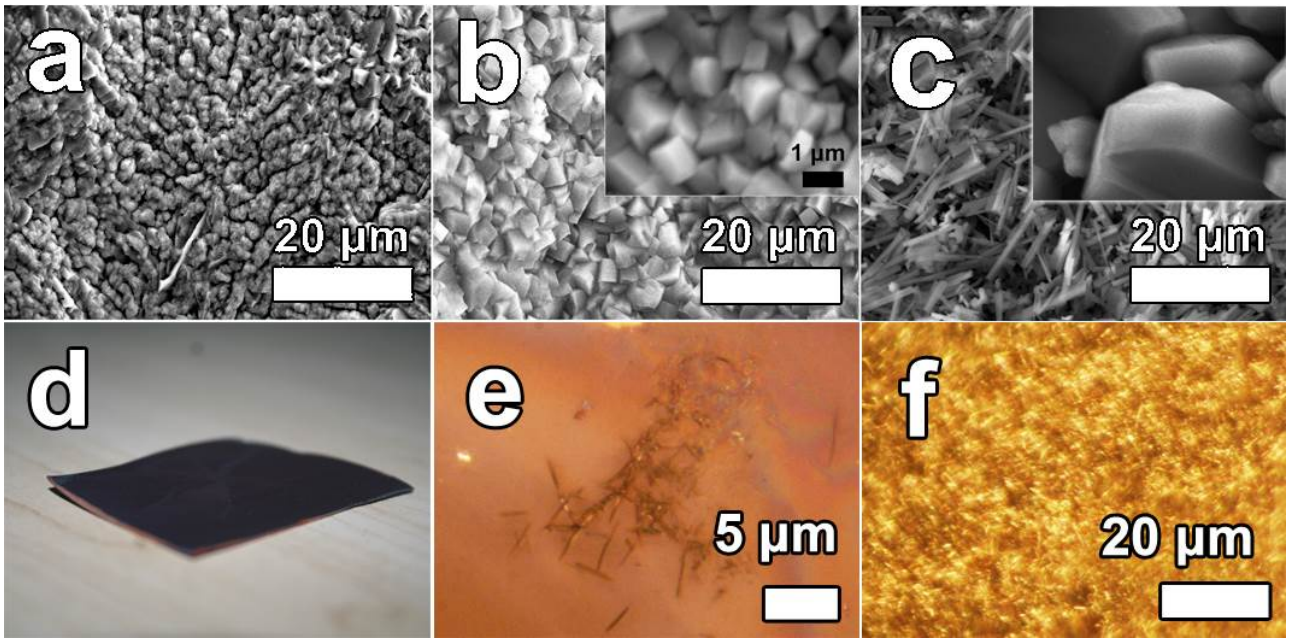

Figure S2. Scanning electronic microscope images of the Cu foil annealed at 250°C (a), 350°C (b), and 550°C (c), digital images (d) and microscopic images of the Cu foil annealed at 450°C (e and f).

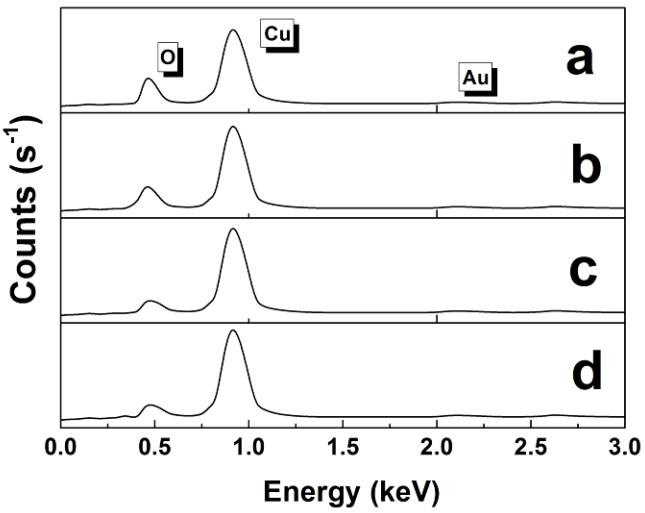

Figure S3 Energy dispersive X-ray spectra (EDS) of the Cu foil annealed at 250°C (a), 350°C (b), 450°C (c), and 550°C (d). The atomic ratio of Cu:O rose from 1.02:1 (a) to 1.54:1 (b), 1.98:1 (c) and 1.99:1 (d) with the increase of the annealing temperatures.

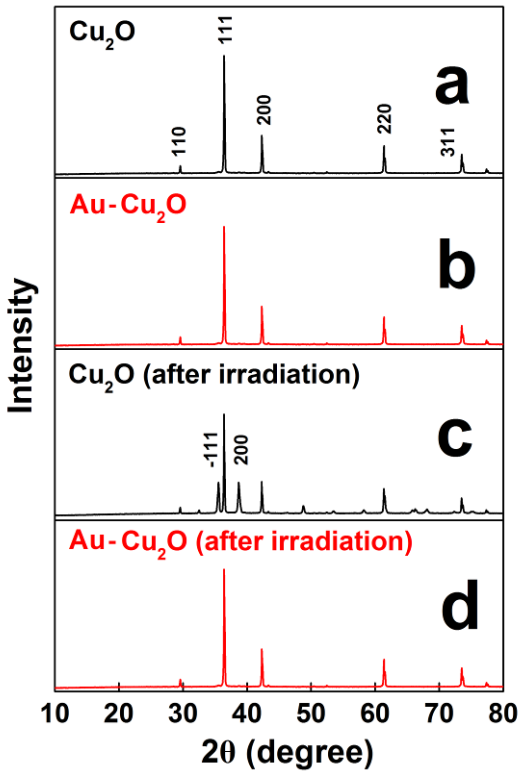

Figure S4. The X-ray diffraction analysis on the Au-Cu_2O NWAs and Cu_2O NWAs before and after photocatalytic experiment.

Mechanism of Cu_2O rod formation. The similar mechanism has been proposed by Yue et al. [4] When the polished Cu foil was placed in air, the surface of the Cu foil was oxidized and covered with a layer of Cu_2O. Treated by annealing, the Cu_2O layer experienced thermal expansion. In the early annealing process, the surface diffusion of Cu atoms near the Cu_2O/Cu interface was caused by the stress concentrations, which occurred at the grain boundaries due to material singularities. When the diffusion rate was high enough and the accumulation of Cu atoms at the Cu_2O/Cu interface reached a critical value, the packed Cu atoms penetrated the Cu_2O layer (Figure S5a), and stacked into nanowires, as shown in Figure S5b. The growth of nanowires relieved parts of compressive stresses near the Cu_2O/Cu interface, and the stress gradient between the top (Cu_2O side) and bottom (Cu side) faces of the Cu foil was generated. The higher the annealing temperature, the larger stress gradient. To relieve the compression stresses in the Cu_2O/Cu interface, the Cu_2O nanowires, prisms, and rods grew along the axial direction, depending on the different stress gradient. The growth of these rods continued until the local tensile stress disappeared.

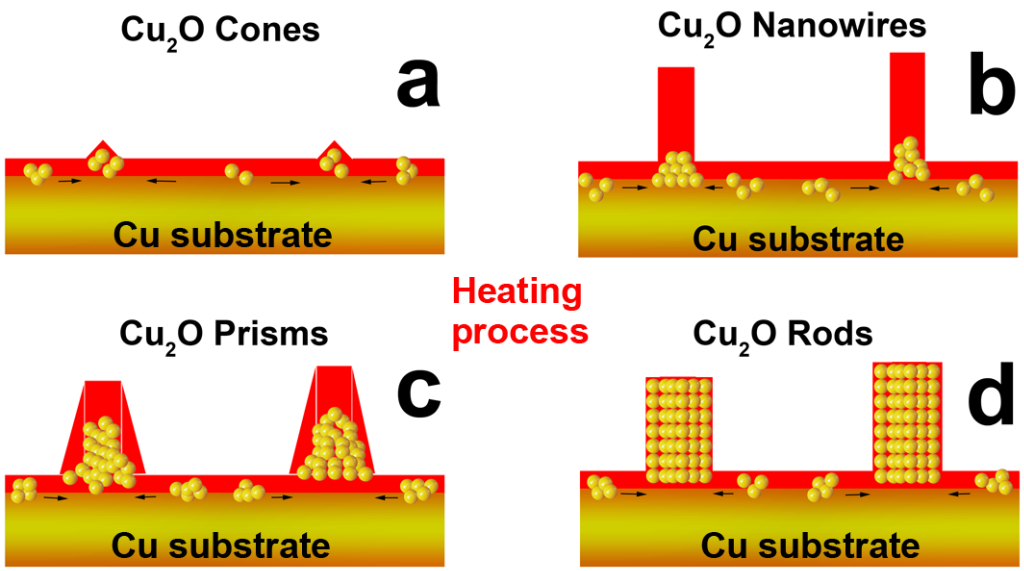

Figure S5. The schemes of Cu_2O grown from cones to wires, prisms, and rods.

Photoabsorptivity. The as-fabricated Au-Cu_2O NWAs exhibited highly tunable optical properties in the visible and near infrared regions. The corresponding experimental results of diffuse reflectance spectra (DRS, Figure S4) shows the complicated optical features of Au-Cu_2O NWAs combining Cu_2O NWAs and Au nanoparticles (Au NPs). The plasmon resonance phenomenon was observed after Au coating, and the results showed that the photoabsorption edge shifted to longer wavelength. These results were similar with previous studies that coating the Au [5] or Ag [6] nanoparticles onto semiconductors led to the redshift of the absorption edge by several tens of nanometers. Theoretically, the band gap energy of a semiconductor could be calculated by the following Equation [7]:

$$\alpha h\nu = A(h\nu - E_g)^{n/2} \quad (1)$$

where α, h, ν, E_g, and A are absorption coefficient, Planck constant, light frequency, band gap, and a constant, respectively. The value of n depends on the characteristics of the transition in a semiconductor, i.e., direct transition (n=1) or indirect transition (n=4). For Cu_2O, the value of n is 1 for the direct transition [8]. Therefore, the band gap energy (E_g value) of the samples can be estimated from a plot of $(\alpha h\nu)^{1/2}$ versus photon energy ($h\nu$). The intercept of the tangent to the X axis would give a good approximation of the band gap energy of the samples. The absorption edges for the samples were apparent, at λ = 577 nm for Cu_2O NWAs (E_g = 2.17 eV) in agreement with previously reported values [9], and at λ = 780 nm for Au-Cu_2O NWAs (E_g = 1.59 eV). As shown in Figure S6, the Au-Cu_2O NWAs showed an increased absorption between 480 and 800 nm as compared to the Cu_2O NWAs. The spectral features on the red side of 560 nm could be most reasonably assigned to the plasmon resonances of coated-Au layer whose frequencies red-shifted from 560 nm for the bare Au

NPs [10]. The absorption of Au-Cu_2O NWAs in the region 400–800 nm shared similarities with the characteristics spectral of sunlight [11], which enabled the Au-Cu_2O NWAs to take full advantage of radiation energy in sunlight.

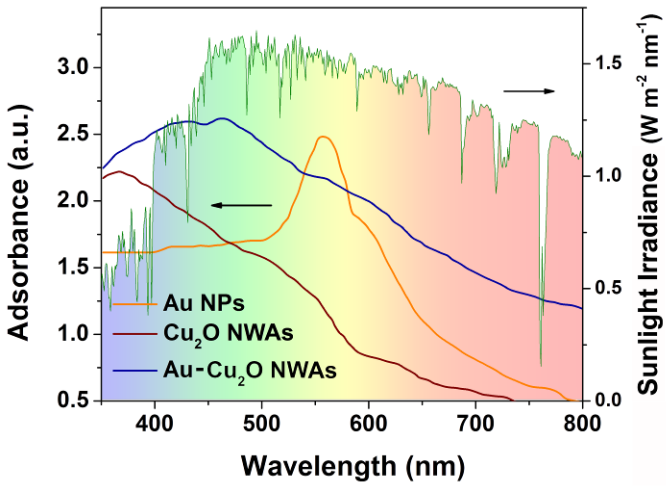

Figure S6. Diffuse reflectance spectrophotometry (DRS) of Cu_2O NWAs, Au-Cu_2O NWAs and Au nanoparticles (NPs), and reference sunlight radiation (AM1.5) from simple model of the atmospheric radiative transfer of sunshine (SMARTS).

TOC destruction under visible light and UV light. As shown in Figure S7, the TOC removal efficiency of TCS under visible light irradiation was less than that under UV-light irradiation. Actually, photocatalytic reduction failed to mineralize TCS due to the moderate dechlorination process. However, that made it possible for photocatalytic reduction to detoxify TCS in a safer way.

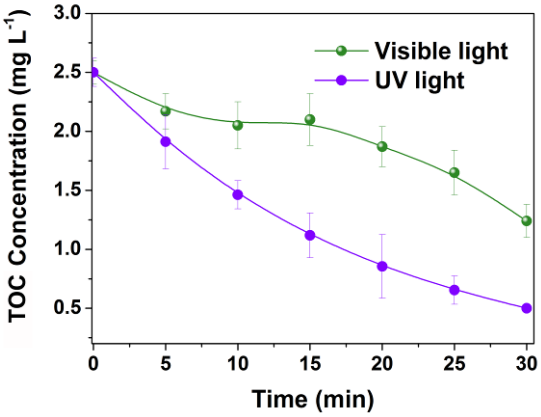

Figure S7. The TOC concentration of TCS as a function of reaction time by photocatalytic degradation with Au-Cu_2O NWAs under the irradiation of visible light and UV-light.

Kinetics. The kinetics of photocatalysis was studied to better understand the degradations of TCS on the Cu_2O NWAs and Au-Cu_2O NWAs, at pH 6.5 and constant temperature of 25°C. Initial concentrations of TCS (C_0) were 5.0 mg·L^{-1} and photocatalyst dosage was 50 cm^2.

The photocatalytic reaction followed first-order kinetics in following Equation [12].

$$ln(C/C_0) = -kt \quad (2)$$

where C and C_0 are the concentrations of TCS, and k is the reaction rate constant at a certain temperature.

The degradation rates of TCS on the Cu_2O NWAs and Au-Cu_2O NWAs under photocatalysis were 0.005 min^{-1} and 0.238 min^{-1}, respectively. The differences in two degradation rates could be explained by the different activities of photocatalysts. Obviously, the degradation rate on Au-Cu_2O NWAs was faster than that on Cu_2O NWAs, by 47.6 times.

Quantum yield of degradation. Photocatalytic experiments were conducted to calculate the quantum yield rate of Au-Cu_2O NWAs, by two different methods.

The integral quantum yield is:

$$\Phi = (\text{number of events})/(\text{number of photons absorbed}) \quad (3)$$

For a photochemical reaction:

$$\Phi = (\text{amount of reactant consumed})/(\text{amount of photons absorbed}) \quad (4)$$

The differential quantum yield is:

$$\Phi = \mathrm{d}[x]/n \cdot \mathrm{d}t \quad (5)$$

where d[x]/dt is the change rate of a measurable quantity, an n is the amount of photons (mol or its equivalent Einstein) absorbed per unit time.

By this means, the quantum yield of TCS degradation by the Au-Cu_2O NWAs photocatalyst could be calculated by the integrated intensity distribution curve and the removed TCS concentration. Considering the photoabsorptivity of Au-Cu_2O NWAs and the use of cut-off filter, the illumination energy of Xenon lamp could be divided into two parts: the light removed by the filter and light that is absorbed by the photocatalyst. They were 32.1 and 164.1 mW cm^{-2} nm^{-1}, respectively (see the Figure below). The energy of a photon is given by the Equation:

$$E = hc/\lambda \quad (6)$$

where h is the Planck constant, c is the velocity of light, and λ is the wavelength of the light. The photon flux of "absorbed" area (see Figure S8) could be calculated by conversion from the intensity of irradiation. Therefore, the average quantum yield efficiency can be calculated as 0.012 [TCS removed]/[photon] during first 10 min of the reaction. The energy efficiency was 0.02 mg W^{-1} h^{-1}.

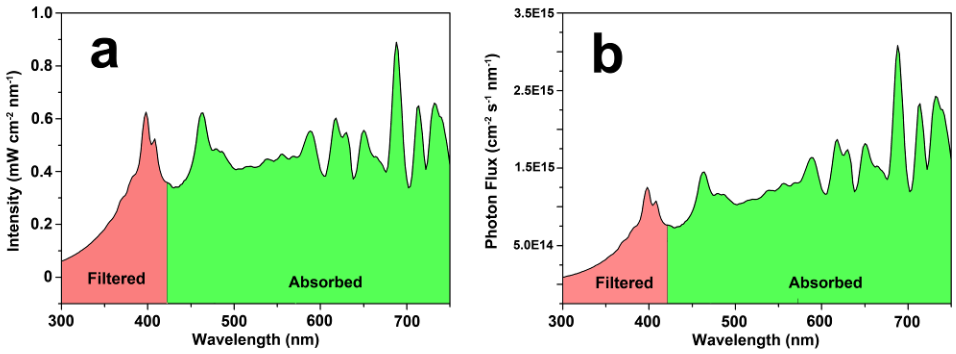

Figure S8. Luminous intensity distribution curve (a) and photon flux (b) of the Xenon lamp used in the photocatalytic experiments. The irradiation area of the photocatalytic reactor was 50.24 cm^2.

To estimate the response of Au-Cu_2O NWAs under different wavelength light irradiation, we design a new setup to measure the reactive activity of Au-Cu_2O NWAs. Firstly, we purchased a series of laser generator with wavelength of 395nm, 405 nm, 532nm, and 650 nm. The laser light was excited to illuminate a quartz micro-cuvette containing only 100 μL of TCS solution (5.0 mg L^{-1}). Because the excellent monochromaticity of laser, the quantum yield for different wavelengths could easily measured for these wavelengths.

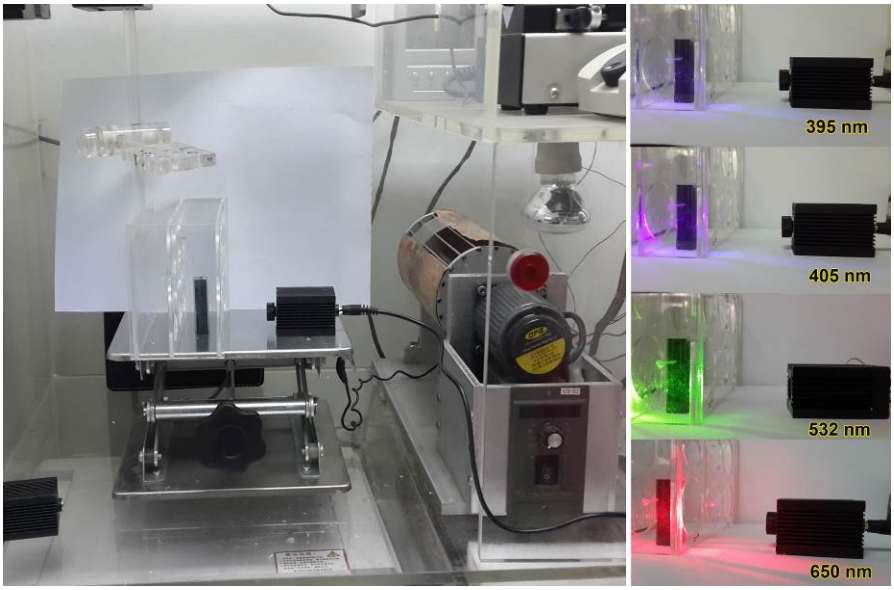

Figure S9. The setup for measuring quantum yield of Au-Cu_2O NWAs under the irradiation of laser light with different wavelengths (395 nm, 405 nm, 532 nm, and 650 nm).

Using this method, the quantum yield rate of Au-Cu_2O NWAs for wave length of 395 nm, 405 nm, 532 nm, and 650 nm were found to be 0.16, 0.25, 0.08, and 0.002 [TCS destroyed]/[photon], respectively.

Optimum amount of Au. As shown in Figure S10, the relative activity of Au-Cu_2O NWAs for the degradation of TCS increased up to a beam sputtering time of 36, and then decreased with in increase of sputtering time. The coating layer thickness increased with increasing function of IBS time. The thickness of Au layer was determined to be about 10.5 nm after 30 s of IBS. The optimum amount can be explained is the result of a tradeof. At lower Au content less electrons are transfered to the Au might and more recombinations of holes and electrons would occur and lower photocatalytic activity would be observed. At high Au content, the Au would shield photocatalyst from light and diminished the quantum efficiency. Consequently, we see the trend in Fig. S10.

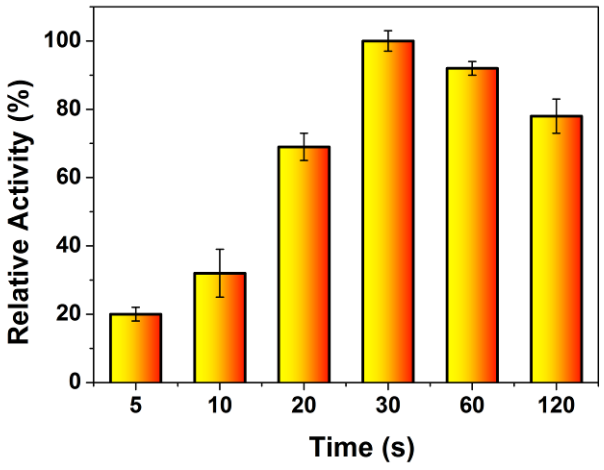

Figure S10. The relative activity of Au-Cu_2O NWAs for the degradation of TCS as a function of ion beam sputtering (IBS) time.

Catalytic role of gold. We conducted the photocatalytic experiments for the degradation of TCS with Au foil, nano-Au particles (with diameter of 5 nm and 20 nm from Cytodiagnostics, CA), and ion sputtered nano-Au layer on glass. As shown in Figure S11, little TCS was degraded by Au photocatalysis in the reaction time as long as 2 h, regardless with UV light or visible light were used. Of course, we found some UV-photolysis. Therefore, it is safe to say that Au was not responsible for the removal of TCS by its photocatalysis (or surface adsorption). In other word, the coated Au acted as a promoter, or a cocatalyst to enhance the photocatalytic activity of Cu_2O, rather than as a photocatalyst.

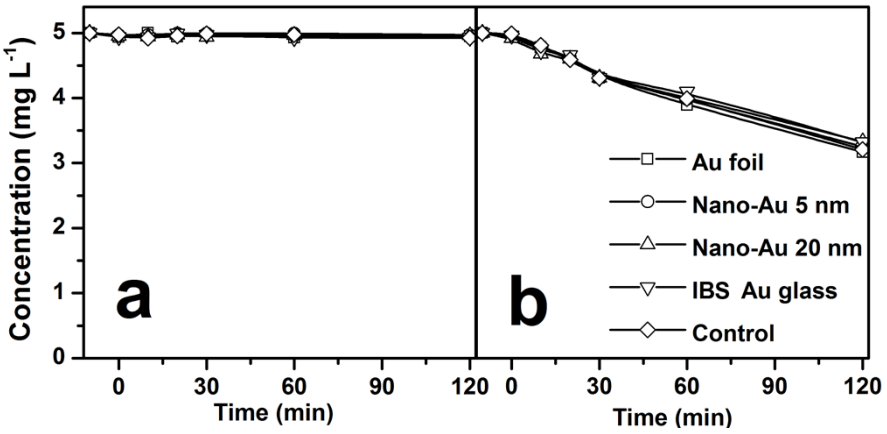

Figure S11. The TCS concentration profile as a function of reaction time in the presence of Au foil, nano-Au particles (with diameter of 5 nm and 20 nm), nano-Auon glass by ion beam sputtering (IBS Au glass) under the irradiation of visible light (>420 nm, a) and UV light (b).

DCDDs and DCHDFs. In the presence of Au-Cu_2O NWAs, regardless of under UV-light or visible light irradiation, the photocatalytic reduction was dominated the reaction pathway. In a reductive environment, TCS tended to be dechlorinated and transformed into phenoxyphenol, which is not be precursor of DCDDs or DCHDFs in the absence of sufficient halogenating reagents. A

similar conclusion was also found in the reduction of TCS by analogical approaches, including electrochemical, biological, and zero-valence metallic reduction processes [13-16].

By contrast, TiO_2/UV-light driven photocatalyst has a powerful oxidation potential and can produce hydroxyl radical and the photocatalytic oxidation is the main reaction. It has been reported that the ·OH radical prefers to attack the para-position of phenol part in TCS [17-19], break TCS into two phenolic groups or cleave one chlorine group and form phenoxyl radicals. As a result, the two rings linked with each other by C-O-C or C-C bands and DCDDs or DCHDFs are generated.

Based on the above discussion, two conditions need to be satisfied for the formation of DCDDs and DCHDFs. First, it is critical to produce highly active ·OH for the cleavage and oxidation. Second, the chlorinated phenoxyphenols should not be dechlorinated before it react with ·OH. For our visible photocatalyst, ·OH has not been detected. And TCS and chlorinated phenoxyphenols were rapidly dechlorinated by photocatalytic reduction, and could no longer act as the precursor of DCDDs and DCHDFs. Also, if even a little of DCDDs or DCHDFs was generated with the visible light photocatalyst solution, they would be reduced and dechlorinated. Therefore, it is safe to say that there is little chance for such a photocatalytic reduction process to produce DCDDs and DCHDFs.

ESR analysis. We employed the ESR technique to detect the reactive species generated by Au-Cu_2O NWAs under light irradiation at λ 532 nm and 355 nm. The results verified the absence of hydroxyl radicals (•OH) and singlet oxygen ($^1O_2$). As shown in Figure S12, •OH could not be detected in the solution under the irradiation of UV-light (λ 355 nm) and visible light (λ 532 nm), which was different from the well-known photocatalytic oxidation mechanism for UV-light responsive

photocatalysts. $^1O_2$ was not detected as well. However, O_2^- was detected in the experiments, with a strong signal and may result be from reduction of O_2 (See Equation 8).

$$\text{photocatalyst} + h\upsilon \rightarrow e_{cb}^- + h_{vb}^+ \quad (7)$$

$$e_{cb}^- + O_2 \rightarrow O_2^- \quad (8)$$

$$h_{vb}^+ + OH^- \rightarrow \bullet OH \quad (9)$$

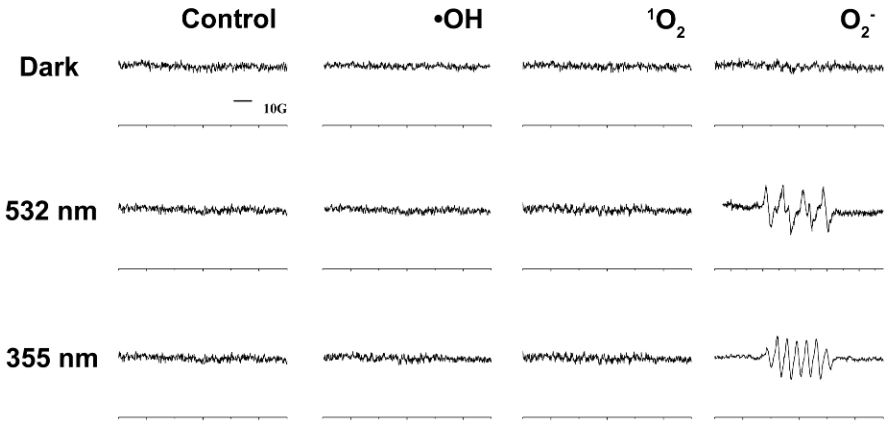

Figure S12. ESR signals for detecting •OH, $^1O_2$ and O_2^- in the presence of Au-Cu_2O NWAs, under irradiation at λ 532 nm and 355 nm.

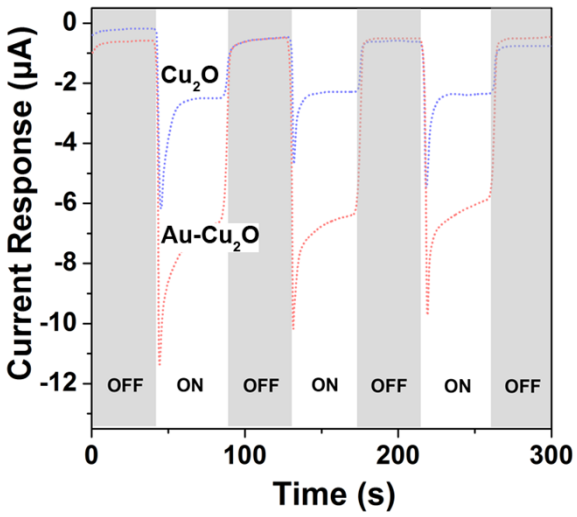

Figure S13 The photocurrent of the Cu_2O NWAs and Au-Cu_2O NWAs alternately irradiated by visible light (>420 nm) and sheltered every 45 s (Light ON and OFF in the Figure).

Frontier Molecular Orbit. For a redox reaction, the potentials of electron-donating (reductive capacity) and electron-accepting (oxidative capacity) are crucial, but difficult to measure experimentally due to the complex chemical equilibrium [20]. Recently, computational chemistry has been employed for calculating the redox potentials of different species. Density functional theory (DFT) has played a predominant role in this evolution. In this study, the redox potentials of TCS were calculated with the employment of ab initio methods. The energies of the lowest unoccupied molecular orbital (LUMO) and highest occupied molecular orbital (HOMO) of the TCS were calculated. The HOMO represents the ability to donate an electron while LUMO represents the ability to obtain an electron [21].

The LUMO and HOMO diagrams in ground state are shown in Figure S7. Gaussian 03 was used for the DFT calculation of TCS. The geometries were optimized at the B3LYP (Becke's three parameter hybrid method with LYP correlation). The 6-31G basis set was used for structural optimization of TCS [22]. All the calculations have been performed on Red Hat Linux 5.5 platform.

It can be seen that LUMO frontier orbitals spread over the whole π-conjugated backbone, and reside on the central of C2, C3, and C5, which have been marked as the active sites for the nucleophilic attack by electrons or hydrated electrons. Therefore, the Cl group conjoined with C2 atoms is liable to cleave from the rings. By this means, the dechlorination products of TCS can be predicted selectively from the isomers of them.

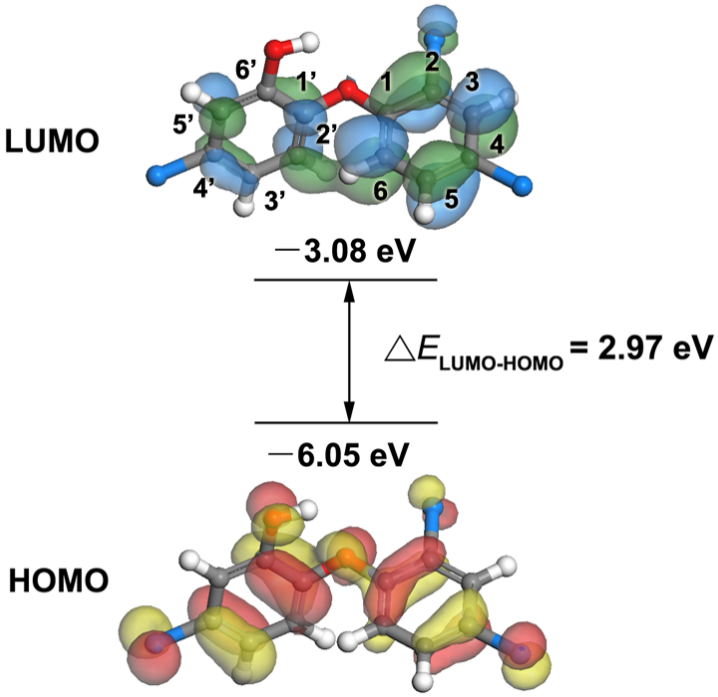

Figure S14. Contour plots of the frontier molecular orbitals, including HOMO (highest occupied molecular orbital) and LUMO (lowest unoccupied molecular orbital) of TCS. The color and size of the lobes reflect the sign and amplitude of the LCAO (linear combination of atomic orbitals) coefficients, respectively. The energy level of HOMO and LUMO, and the energy gap between HOMO and LUMO ($\Delta E_{\mathrm{LUMO-HOMO}}$) are listed as well. Blue/green and red/yellow ellipsoids represent LUMO and HOMO electron cloud of (+/–) wave-function phase, respectively.

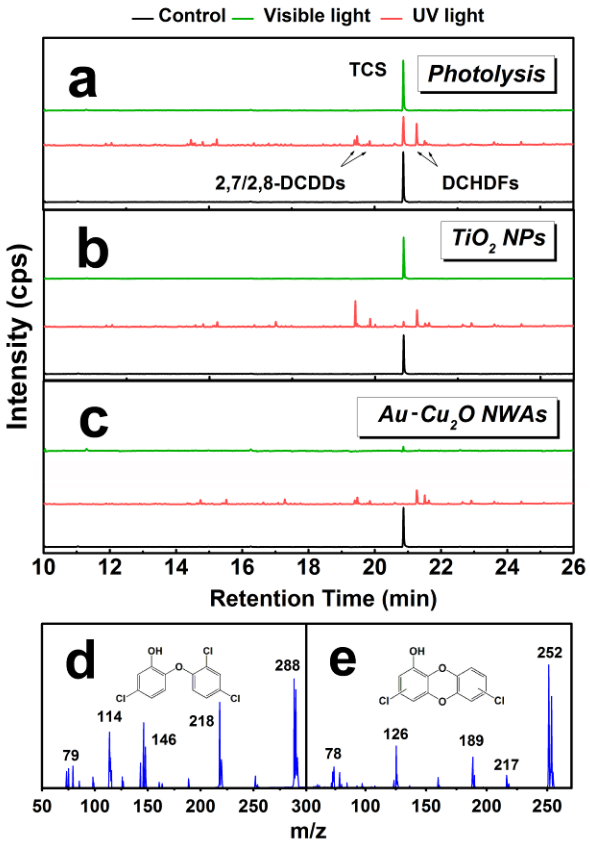

Figure S15. GC-MS selected ion monitoring (SIM) spectra of TCS degradation by photolysis (a), TiO_2 NPs photocatalysis (b) and Au-Cu_2O NWAs photocatalysis (c) after 30 min, and the mass spectra of TCS (d) and 2,7/2,8-dichlorodibenzodioxin (e). The control tests for all experiments were carried out in dark.

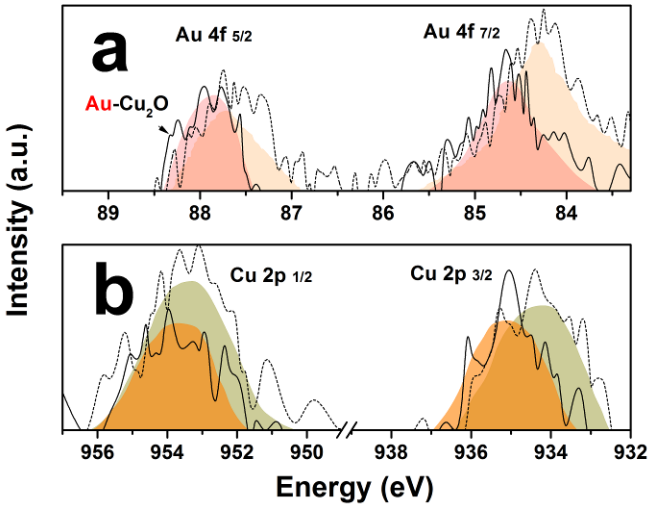

Figure S16. XPS spectra of Au 4f 5/2, Au 4f 7/2, Cu 2p 1/2 and Cu 2p 3/2 from the surface of the Au nanoparticles, Cu_2O NWAs and Au-Cu_2O NWAs. Solide line and dash line in Figure S16a

represent Au in Au-Cu_2O and nano-Au; Solide line and dash line in Figure S16b represent Cu in Au-Cu_2O and Cu_2O, respectively.

Work Functions. To track the energy band changes of Au, Cu_2O, and Cu, their work functions under different conditions should be measured at first. Generally, when a metal and a semiconductor are in contact, the free electrons will transfer between them due to the different level of work function. The electron transfers continuously until the Fermi energy levels of metal (E_F, m) and semiconductor (E_F, s) are aligned through raising one and lowering the other. Therefore, the work fucntions of the contacted two sides (metal and semiconductor) should be equal. Therefore, we tried to measure the work function of independent Au nanoparticles and Au nanoparticles coated on the Cu_2O NWAs, the Cu_2O NWAs (scraped from the Cu foil) and Cu_2O NWAs on Cu foil, pure Cu foil and Cu foil with Au-Cu_2O NWAs. We expect these measurements and comparisons could reflect the energy band change during the preparation of Au-Cu_2O NWAs on Cu foil.

As shown in Figure S17, Ultraviolet photoelectron spectroscopy (UPS) was taken to measure the work functions of Au, Cu_2O, and Cu foil under different conditions. The cutoff energy (E_{cutoff}) and Fermi energy (E_{Fermi}) are determined by linear extrapolation to the zero of the profiles. The work function can be calculated from the UPS using the Equation (10) [23, 24]:

$$\Phi = h\nu - E_{cutoff} + E_{Fermi} \quad (10)$$

where $h\nu$ (=21.22 eV) is the incoming photon energy from He I source; E_{cutoff} is the energy of cutoff edge; E_{Fermi} is the energy at Fermi energy level. As shown in Figure S17a, the E_{cutoff} of the independent Au nanoparticle and that coated on the Cu_2O NWAs is 16.05 eV and 16.60 eV, respectively, and both of their E_{Fermi} are close to 0 eV. Accordign to the Equation (10), the work

function of the independent Au nanoparticle and that coated on the Cu_2O NWAs is 5.17±0.05 eV and 4.62±0.05 eV, respectively. Thus, the Au nanoparticles showed the lower work function (i.e. higher Fermi energy level) after coated onto the Cu_2O NWAs, which could be attributed to the electrons pouring into the energy band of Au. Considering the only contact between Au and Cu_2O, we believe the electrons must come from Cu_2O side.

As shown in Figure S17b, the work function of Cu_2O NWAs scraped from the Cu foil (5.06±0.05 eV) was higher than that on Cu foil (4.67±0.05 eV). However, the work function of Cu was nearly invariable (4.62±0.05 eV), regardless with or without NWAs on it (see Figure S17c). Apparently, the electrons of Cu migrated into the energy band Cu_2O after Cu_2O/Cu contact.

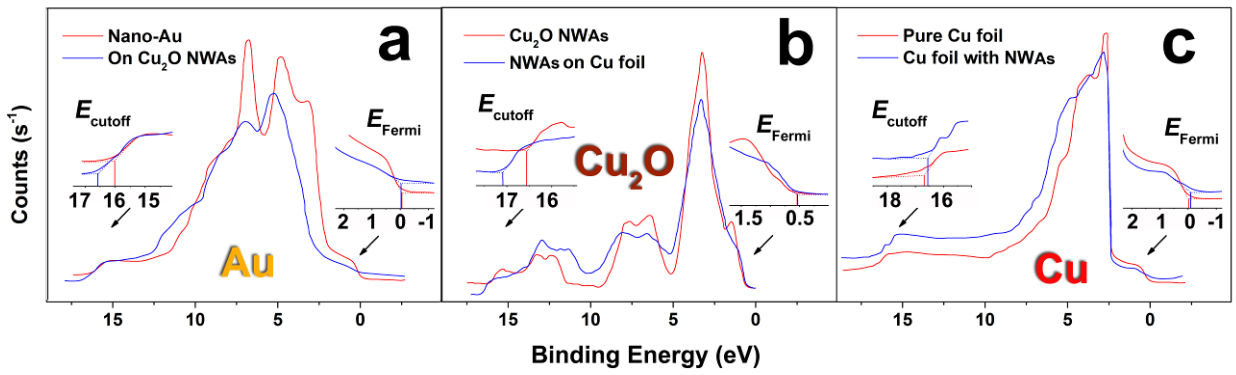

Figure S17. Ultraviolet photoelectron spectroscopy (UPS) of independent Au nanoparticles and Au nanoparticles coated on the Cu_2O NWAs (a), Cu_2O NWAs and Cu_2O NWAs on Cu foil (b), pure Cu foil and Cu foil with Au-Cu_2O NWAs (c). The profile of Cu foil with Cu_2O NWAs was similar to that with Au-Cu_2O NWAs, and was omitted in the Figure.

The work functions of Cu_2O and Cu were measure by UPS and the increase of the Fermi energy level of Cu_2O was founded after contact with Cu. Next, the height of the Schottky barrier was analyzed on Keithly 2400 source measuring unit (USA) and CHI 660D electrochemical workstation (CHN). As shown in Figure S18, the current profile was rendered as a function of voltage. The Schottky barrier can be calculated based on the thermionic emission theory (TET).

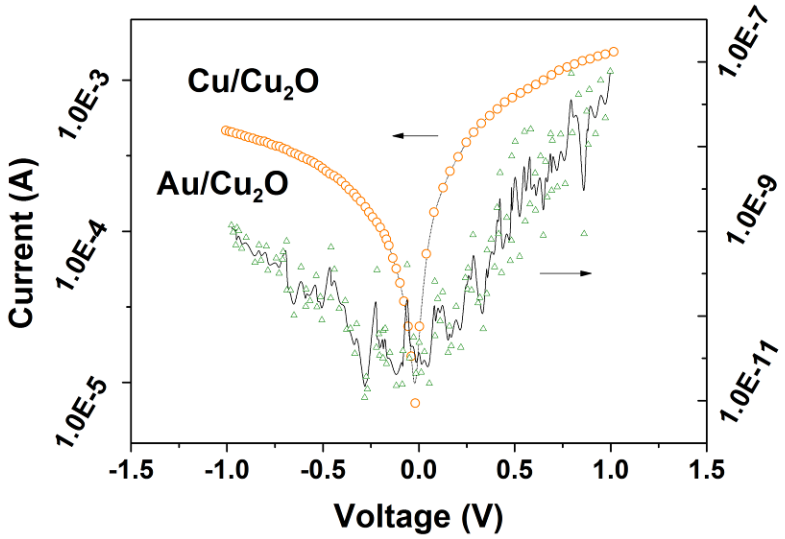

Figure S18. The current as a function of applied bias potential obtained on the Au-Cu_2O NWAs by electrochemical workstation (for Cu/Cu_2O) and atomic force microscopy (for Au/Cu_2O).

Under the positive bias voltage, the correlation between current and voltage can be expressed as:

$$I = SAT^2 \exp\left(-\frac{q\phi_{ns}}{k_0 T}\right)\left(\exp\left(\frac{qV}{nk_0 T}\right) - 1\right) \quad (11)$$

where I is the current, S is the surface area of the plates, A is the Richardson constant, q is the electronic charge, φ_{ns} is the height of the Schottky barrier, k_0 is the Boltzmann constant, V is the applied bias voltage, and n is the ideality factor.

When the $V<k_0T/q$, the equation (11) can be simplified into:

$$I = SAT^2 \exp\left(-\frac{q\phi_{ns}}{k_0 T}\right)\left(\exp\left(\frac{qV}{nk_0 T}\right)\right) \quad (12)$$

and

$$\ln I = \frac{qV}{nk_0 T} + \ln\left(SAT^2\right) - \frac{q\phi_{ns}}{k_0 T} \quad (13)$$

From the equation (12) and (13), the height of the Schottky barrier (φ_{ns}) was measure to be 0.42 eV by linear fitting I-V profiles. Obviously, the difference between the work functions of Cu and Cu_2O resulted in the directional flow of electrons from Cu to Cu_2O, which built a typical Schottky barrier.

We also tried to measure the band bending in the space charge layer between Au and Cu_2O. However, it is difficult to obtain the I-V profile on the Au-Cu_2O NWAs surface, because the Au was coated on the Cu_2O NWAs which grew in all shapes and sizes. The thickness of the Au layer on different NWs is uneven. We tried several times and failed to obtain a steady curve by using the electrochemical methods. Therefore, we utilized the AFM (SEIKO SPA-300HV, JPN; Operating mode: Non-contact, tip size <10 nm) to measure it (Figure S18 and S19). The height of the barrier was calculated to be 0.027 eV. The abnormal results might be due to the nano-scale layer of Au where the energy levels are very discrete. However, the thickness of the Au layer should be measure by an accurate approach.

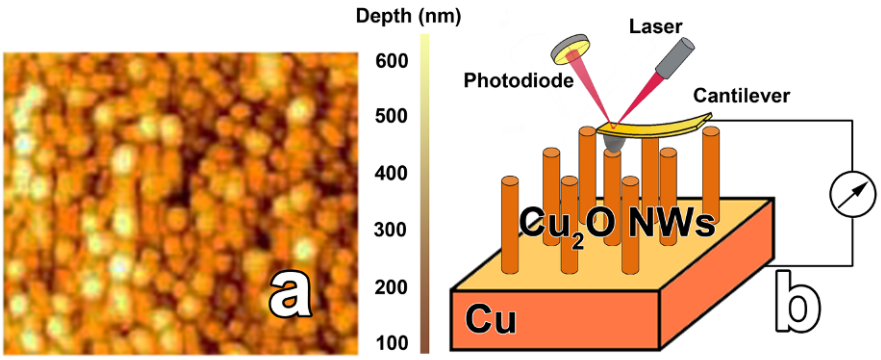

Figure S19. The AFM image (a) and the schematic diagram for measuring the I-V profile of Au-Cu_2O NWs on the Cu foil.

The thickness of Au layer was investigated by XPS recorder with argon etching. Because the etching rate of Au element was known as 0.35 nm s^{-1} [25], the thickness of Au layer can be calculated by measuring the etching time until new dominating elements (Cu or O in our case) was detected. As shown in Figure S20, the Au layer was eliminated after about 30 s after argon etching. The thichness of Au layer (D_L, nm) can be estimated by calculating the product of etching speed (A_e, nm s^{-1}) and etching time (T_e, s):

$$D_L = A_e \times T_e \tag{14}$$

The average thickness of Au layer was about 10.5 nm and the differentiated Au/Cu layers can be well identified from Figure S20.

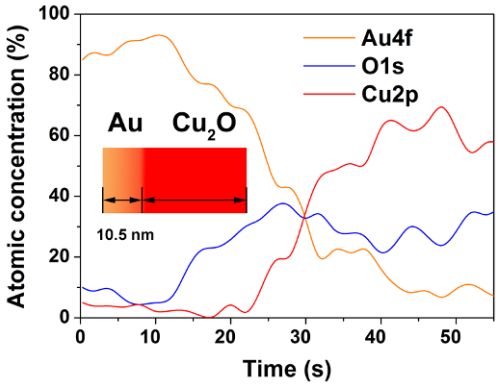

Figure S20. The distribution of Au, O, and Cu elements measured by X-ray photoelectron spectroscopy (XPS) in the vertical direction of Au-Cu_2O NWAs.

For a bulk Au, the gap between adjacent energy levels are indiscernibility, thus its energy levels are continuous. The electrons are free to flow and make Au a conductor. When the size of the Au particle was reduced to nanoscale, the exciton quantum confinement would result in the discrete energy levels. The energy band might not be applicable (or even wrong) for the nano-Au layer on Cu_2O NWAs. Therefore, it is impossible to accurately measure the band bending in the space charge layer between nano-scale Au and Cu_2O NWs.

The width of the depletion layers of Au/Cu_2O and Cu_2O/Cu were measured by C-V method. Herein, the barrier capacitance can be determined by this Equation:

$$C = A\sqrt{\frac{\varepsilon_0 \varepsilon_r qNb}{2(V_d - V)}} \tag{15}$$

where C is the barrier capacitance; ε_r is the relative dielectric constant; A is the contact area; q is the electronic charge; N_b is the carrier concentration; V_d is the contact potential; and V is the bias. The depletion layer thickness is inversely proportional to the square root of the space charge density (N_d) of the layer, which is assumed to be constant, as given by this Equation:

$$\omega = \sqrt{\frac{2\varepsilon_0 \varepsilon_r V_b}{qN_d}} \tag{16}$$

The depletion layer thickness of Cu_2O/Cu was estimated to be about 224 nm, when the density of carriers was 0.67×10^{20} cm^{-3}.

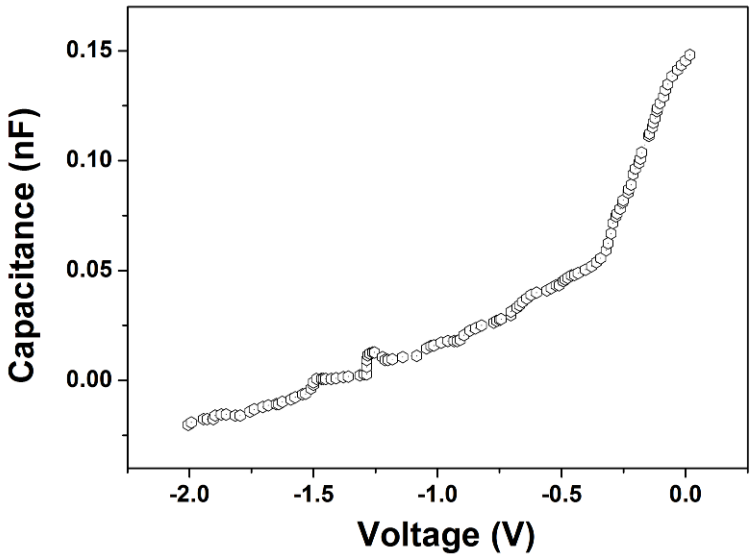

Figure S21. The capacitance-voltage (C-V) characteristics for the Cu_2O/Cu Schottky junction measured at 50 kHz.

***E*$_{LUMO}$ of TCS.** The calculations were performed using the spin-unrestricted Kohn-Sham method. The exchange-correlation function was the B3LYP. The physical wave functions were expanded in terms of accurate numerical basis sets. The numerical basis sets minimized the basis set super position error (BSSE). All atoms were treated with all electron basis sets. The tolerances of energy, gradient, and displacement convergence were 1.0×10^{-5} Hartree, 1.0×10^{-3} Hartree/Å and 0.5×10^{-2} Å, respectively.

The energy level of HOMO and LUMO (E_{HOMO} and E_{LUMO}), and the energy gap between HOMO and LUMO ($\Delta E_{LUMO-HOMO}$) are listed in Figure S14. E_{HOMO} and E_{LUMO} indicated the electronic ionization potential and electron affinity under the energy excitation, respectively [26]. That is to say, E_{LUMO} accounts for the electron accepting capacity and E_{LUMO} represents the electron donating capacity. Herein, E_{HOMO} and E_{LUMO} of TCS were estimated to be –6.05 eV and –3.08 eV, respectively. Therefore, TCS can only be reduced by electron donator with redox potential higher than –3.08 eV. In our case, the electron donators were photo-generated electrons.

Charge transfer direction upon irradiation. Based on the above experimental results, the electron structure and a possible charge transfer mechanism in the Cu/Cu_2O contacts are proposed as shown in Figure 5 in the manuscript. The Fermi level of Cu_2O is located at a more negative level than that of Cu metal. When Cu_2O is in contact with Cu, the band structure of Cu_2O (both the valence band (VB) and the conduction band (CB)) is bent as shown in Figure 5b. Under irradiation, excitation of electrons from the VB to CB in the Cu_2O takes place, leaving holes in the VB. The electron and the hole form an excited electron-hole pair, which is usually short-lived and recombines if there is no driving force to separate them. However, when the electron was accumulated in the Au/Cu_2O and Cu_2O/Cu layer, the photoexcited electrons from Cu_2O are driven by the electric field to the Au core, while holes migrate to the Cu, thus the holes and the electrons can be separated. The electrons reach at the surface of Au and reacted with absorbed electron donator. In this case, the coated Au layer acts as a directional conductive pathway, which allows the charge to transport quickly and effectively, thus the adverse reactions (recombination and back reaction) are suppressed. The holes combined with electrons from the bulk Cu. Compared with the microscopic NWAs, Cu foil can be viewed as a "pool" which supplied abundant electrons. As a sequence, the holes will not accumulate in the VB of Cu_2O. Therefore, the photo-etching of holes was eliminated, which promise the favorable stability of Au-Cu_2O NWAs.

Literature Cited

1. Ryu, J.; Choi, W. Y., Photocatalytic oxidation of arsenite on TiO_2: Understanding the controversial oxidation mechanism involving superoxides and the effect of alternative electron acceptors. *Environ. Sci. Technol.* **2006,** *40*, (22), 7034−7039.

2. Ryu, J.; Choi, W., Effects of TiO_2 surface modifications on photocatalytic oxidation of arsenite: The role of superoxides. *Environ. Sci. Technol.* **2004,** *38*, (10), 2928−2933.
3. Kobayashi, M.; Sakamoto, Y., Singlet oxygen quenching ability of astaxanthin esters from the green alga Haematococcus pluvialis. *Biotechnol. Lett* **1999,** *21*, (4), 265−269.
4. Yue, Y.; Chen, M.; Ju, Y.; Zhang, L., Stress-induced growth of well-aligned Cu_2O nanowire arrays and their photovoltaic effect. *Scr. Mater.* **2012,** *66*, (2), 81−84.
5. Kong, L. N.; Chen, W.; Ma, D. K.; Yang, Y.; Liu, S. S.; Huang, S. M., Size control of Au@Cu_2O octahedra for excellent photocatalytic performance. *J. Mater. Chem.* **2012,** *22*, (2), 719−724.
6. Wang, Z. H.; Zhao, S. P.; Zhu, S. Y.; Sun, Y. L.; Fang, M., Photocatalytic synthesis of M/Cu_2O (M = Ag, Au) heterogeneous nanocrystals and their photocatalytic properties. *Crystengcomm* **2011,** *13*, (7), 2262−2267.
7. Butler, M. A., Photoelectrolysis and physical properties of the semiconducting electrode WO_2 *J. Appl. Phys.* **1977,** *48*, (5), 1914−1920.
8. Zhang, K. L.; Liu, C. M.; Huang, F. Q.; Zheng, C.; Wang, W. D., Study of the electronic structure and photocatalytic activity of the BiOCl photocatalyst. *Appl. Catal. B-Environ.* **2006,** *68*, (3-4), 125−129.
9. Ng, C. H. B.; Fan, W. Y., Shape evolution of Cu_2O nanostructures via kinetic and thermodynamic controlled growth. *J. Phys. Chem. B* **2006,** *110*, (42), 20801−20807.
10. Zhang, L.; Blom, D. A.; Wang, H., Au-Cu_2O core-shell nanoparticles: A hybrid metal-semiconductor heteronanostructure with geometrically tunable optical properties. *Chem. Mater.* **2011,** *23*, (20), 4587−4598.
11. Searle, N. Z.; Hirt, R. C., Ultraviolet spectral energy distribution of Sunlight. *J. Opt. Soc. Am.* **1965,** *55*, (11), 1413−1414.
12. Michael, I.; Achilleos, A.; Lambropoulou, D.; Torrens, V. O.; Perez, S.; Petrovic, M.; Barcelo, D.; Fatta-Kassinos, D., Proposed transformation pathway and evolution profile of diclofenac and ibuprofen transformation products during (sono)photocatalysis. *Appl. Catal. B-Environ.* **2014,** *147*, 1015−1027.
13. Murugesan, K.; Bokare, V.; Jeon, J. R.; Kim, E. J.; Kim, J. H.; Chang, Y. S., Effect of Fe–Pd bimetallic nanoparticles on Sphingomonas sp. PH-07 and a nano-bio hybrid process for triclosan degradation. *Bioresour. Technol.* **2011,** *102*, (10), 6019−6025.
14. Bokare, V.; Murugesan, K.; Kim, Y. M.; Jeon, J. R.; Kim, E. J.; Chang, Y. S., Degradation of triclosan by an integrated nano-bio redox process. *Bioresour. Technol.* **2010,** *101*, (16), 6354−6360.
15. Wang, S. J.; Wang, X.; Poon, K.; Wang, Y. N.; Li, S. F.; Liu, H. X.; Lin, S. H.; Cai, Z. W., Removal and reductive dechlorination of triclosan by Chlorella pyrenoidosa. *Chemosphere* **2013,** *92*, (11), 1498−1505.
16. Knust, K. N.; Foley, M. P.; Mubarak, M. S.; Skljarevski, S.; Raghavachari, K.; Peters, D. G., Electrochemical reduction of 5-chloro-2-(2,4-dichlorophenoxy)phenol (triclosan) in dimethylformamide. *J. Electroanal. Chem.* **2010,** *638*, (1), 100−108.
17. Liu, H. J.; Cao, X. L.; Liu, G. G.; Wang, Y. L.; Zhang, N.; Li, T.; Tough, R., Photoelectrocatalytic degradation of triclosan on TiO_2 nanotube arrays and toxicity change. *Chemosphere* **2013,** *93*, (1), 160−165.

18. Yang, S. G.; Quan, X.; Li, X. Y.; Sun, C., Photoelectrocatalytic treatment of pentachlorophenol in aqueous solution using a rutile nanotube-like TiO_2/Ti electrode. *Photochemical & Photobiological Sciences* **2006,** *5*, (9), 808−814.
19. Yu, J. C.; Kwong, T. Y.; Luo, Q.; Cai, Z. W., Photocatalytic oxidation of triclosan. *Chemosphere* **2006,** *65*, (3), 390−399.
20. Reynolds, C. A.; King, P. M.; Richards, W. G., Computed redox potentials and the design of bioreductive agents. *Nature* **1988,** *334*, (6177), 80−82.
21. Shukla, M.; Srivastava, N.; Saha, S., Investigation of ground state charge transfer complex between paracetamol and *p*-chloranil through DFT and UV-visible studies. *J. Mol. Struct.* **2012,** *1021*, (0), 153−157.
22. Gnanasambandan, T.; Gunasekaran, S.; Seshadri, S., DFT computations and spectroscopic analysis of *p*-bromoacetanilide. *Spectrochim. Acta A Mol. Biomol. Spectrosc.* **2014,** *122*, 542−552.
23. Kim, S.; Song, M.; Rhee, S., Atomic vapor deposited tantalum carbo-nitride film using TBTDET and hydrogen. *ECS Trans.* **2008,** *16*, (4), 355−362.
24. Cahen, D.; Kahn, A., Electron energetics at surfaces and interfaces: Concepts and experiments. *Adv. Mater.* **2003,** *15*, (4), 271−277.
25. Chang, C. C.; Murarka, S. P.; Kumar, V.; Quintana, G., Interdiffusions in thin-film Au on Pt on GaAs (100) studied with Auger spectroscopy. *J. Appl. Phys.* **1975,** *46*, (10), 4237−4243.
26. Shimada, T.; Hotta, S.; Yanagi, H., Energy-transferred photoluminescence from thiophene/phenylene oligomer thin films. *J. Lumin.* **2008,** *128*, (3), 457−461.